

Shape fluctuations in the ground and excited 0^+ states of ^{30}Mg and ^{32}Mg

Nobuo Hinohara,¹ Koichi Sato,¹ Kenichi Yoshida,^{2,1} Takashi Nakatsukasa,¹ Masayuki Matsuo,² and Kenichi Matsuyanagi^{1,3}

¹*Theoretical Nuclear Physics Laboratory, RIKEN Nishina Center, Wako 351-0198, Japan*

²*Department of Physics, Faculty of Science, Niigata University, Niigata 950-2181, Japan*

³*Yukawa Institute for Theoretical Physics, Kyoto University, Kyoto 606-8502, Japan*

(Dated: September 24, 2018)

Large-amplitude collective dynamics of shape phase transition in the low-lying states of $^{30-36}\text{Mg}$ is investigated by solving the five-dimensional (5D) quadrupole collective Schrödinger equation. The collective masses and potentials of the 5D collective Hamiltonian are microscopically derived with use of the constrained Hartree-Fock-Bogoliubov plus local quasiparticle RPA method. Good agreement with the recent experimental data is obtained for the excited 0^+ states as well as the ground bands. For ^{30}Mg , the shape coexistence picture that the deformed excited 0^+ state coexists with the spherical ground state approximately holds. On the other hand, large-amplitude quadrupole-shape fluctuations dominate in both the ground and the excited 0^+ states in ^{32}Mg , so that the interpretation of ‘coexisting spherical excited 0^+ state’ based on the naive inversion picture of the spherical and deformed configurations does not hold.

PACS numbers: 21.60.Ev, 21.10.Re, 21.60.Jz, 27.30.+t

Nuclei exhibit a variety of shapes in their ground and excited states. A remarkable feature of the quantum phase transition of a finite system is that the order parameters (shape deformation parameters) always fluctuate and vary with the particle number. Especially, the large-amplitude shape fluctuations play a crucial role in transitional (critical) regions. Spectroscopic studies of low-lying excited states in transitional nuclei are of great interest to observe such unique features of the finite quantum systems.

Low-lying states of neutron-rich nuclei around $N = 20$ attract a great interest, as the spherical configurations associated with the magic number disappear in the ground states. In neutron-rich Mg isotopes, the increase of the excitation energy ratio $E(4_1^+)/E(2_1^+)$ [1–3] and the enhancement of $B(E2; 2_1^+ \rightarrow 0_1^+)$ from ^{30}Mg to ^{34}Mg [4–6] indicate a kind of quantum phase transition from spherical to deformed shapes taking place around ^{32}Mg . These experiments stimulate microscopic investigations on quadrupole collective dynamics unique to this region of the nuclear chart with various theoretical approaches; the shell model [7–10], the Hartree-Fock-Bogoliubov (HFB) method [11, 12], the parity-projected HF [13], the quasiparticle RPA (QRPA) [14, 15], the angular-momentum projected generator coordinate method (GCM) with [16] and without [17, 18] restriction to the axial symmetry, and the antisymmetrized molecular dynamics [19].

Quite recently, excited 0^+ states were found in ^{30}Mg [20, 21] and ^{32}Mg [22] at 1.789 MeV and 1.058 MeV, respectively. For ^{30}Mg , the excited 0_2^+ state is interpreted as a prolately deformed state which coexists with the spherical ground state. For ^{32}Mg , from the observed population of the excited 0_2^+ state in the (t, p) reaction on ^{30}Mg , it is suggested [22] that the 0_2^+ state is a spherical state coexisting with the deformed ground state and

that their relative energies are inverted at $N = 20$. However, available shell-model and GCM calculations considerably overestimate its excitation energy (1.4–3.1 MeV) [9, 10, 16, 21]. It is therefore a challenge for modern microscopic theories of nuclear structure to clarify the nature of the excited 0_2^+ states. For understanding shape dynamics in low-lying collective excited states of Mg isotopes near $N = 20$, it is certainly desirable to develop a theory capable of describing various situations in a unified manner, including, at least, 1) an ideal shape coexistence limit where the wave function of an individual quantum state is well localized in the deformation space and 2) a transitional situation where the large-amplitude shape fluctuations dominate.

In this article, we microscopically derive the five-dimensional (5D) quadrupole collective Hamiltonian using the constrained Hartree-Fock-Bogoliubov (CHFB) plus local QRPA (LQRPA) method [23]. The 5D collective Hamiltonian takes into account all the five quadrupole degrees of freedom: the axial and triaxial quadrupole deformations (β, γ) and the three Euler angles. This approach is suitable for our purpose of describing a variety of quadrupole collective phenomena in a unified way. Another advantage is that the time-odd mean-field contributions are taken into account in evaluating the vibrational and rotational inertial functions. In spite of their importance for correctly describing collective excited states, the time-odd contributions are ignored in the widely used Inglis-Belyaev cranking formula for inertial functions. The CHFB + LQRPA method has been successfully applied to various large-amplitude collective dynamics including the oblate-prolate shape coexistence phenomena in Se and Kr isotopes [23, 24], the γ -soft dynamics in sd -shell nuclei [25], and the shape phase transition in neutron-rich Cr isotopes [26]. A preliminary version of this work was reported in Ref. [27].

The 5D quadrupole collective Hamiltonian is written as

$$\mathcal{H}_{\text{coll}} = T_{\text{vib}} + T_{\text{rot}} + V(\beta, \gamma), \quad (1)$$

$$T_{\text{vib}} = \frac{1}{2} D_{\beta\beta}(\beta, \gamma) \dot{\beta}^2 + D_{\beta\gamma}(\beta, \gamma) \dot{\beta} \dot{\gamma} + \frac{1}{2} D_{\gamma\gamma}(\beta, \gamma) \dot{\gamma}^2, \quad (2)$$

$$T_{\text{rot}} = \frac{1}{2} \sum_{k=1}^3 \mathcal{J}_k(\beta, \gamma) \omega_k^2, \quad (3)$$

where T_{vib} and T_{rot} are the vibrational and rotational kinetic energies, respectively, and V is the collective potential. The vibrational collective masses, $D_{\beta\beta}$, $D_{\beta\gamma}$, and $D_{\gamma\gamma}$, are the inertial functions for the (β, γ) coordinates. The rotational moments of inertia \mathcal{J}_k associated with the three components of the rotational angular velocities ω_k are defined with respect to the principal axes. In the CHF + LQRPA method, the collective potential is calculated with the CHF equation with four constraints on the two quadrupole operators and the proton and neutron numbers. The inertial functions in the collective Hamiltonian are determined from the LQRPA normal modes locally defined for each CHF state in the (β, γ) plane. The equations to find the local normal modes are similar to the well-known QRPA equations, but the equations are solved on top of the non-equilibrium CHF states. Two LQRPA solutions representing quadrupole shape motion are selected for the calculation of the vibrational inertial functions. After quantizing the collective Hamiltonian (1), we solve the 5D collective Schrödinger equation and obtain collective wave functions

$$\Psi_{\alpha IM}(\beta, \gamma, \Omega) = \sum_{K=\text{even}} \Phi_{\alpha IK}(\beta, \gamma) \langle \Omega | IMK \rangle, \quad (4)$$

where $\Phi_{\alpha IK}(\beta, \gamma)$ are the vibrational wave functions and $\langle \Omega | IMK \rangle$ are the rotational wave functions defined in terms of \mathcal{D} functions $\mathcal{D}_{MK}^I(\Omega)$. We then evaluate $E2$ matrix elements. More details of this approach are given in Ref. [23].

We solve the CHF + LQRPA equations employing, as a microscopic Hamiltonian, the pairing-plus-quadrupole (P+Q) model including the quadrupole-pairing interaction. As an active model space, the two-major harmonic oscillator shells (sd and pf shells) are taken into account for both neutrons and protons. To determine the parameters in the P+Q Hamiltonian, we first perform Skyrme-HFB calculations with the SkM* functional and the surface pairing functional using the HFBTHO code [28]. The pairing strength ($V_0 = -374$ MeV fm⁻³, with a cutoff quasiparticle energy of 60 MeV) is fixed so as to reproduce the experimental neutron gap of ³⁰Ne (1.26 MeV). We then determine the parameters for each nucleus in the following way. The single particle energies are determined by means of the constrained Skyrme-HFB calculation at the spherical shape. The resulting single particle energies (in the canonical basis) are then scaled with the effective mass of the SkM* functional $m^*/m = 0.79$,

since the P+Q model is designed to be used for single-particle states whose effective mass is equal to the bare nucleon mass. In ³²Mg, the $N = 20$ shell gap between $d_{3/2}$ and $f_{7/2}$ is 3.7 MeV for the SkM* functional, and it becomes 2.9 MeV after the effective mass scaling. This value is appreciably smaller than the standard modified oscillator value 4.5 MeV [29]. This spacing almost stays constant for ^{30–36}Mg. The strengths of the monopole-pairing interaction are determined to reproduce the pairing gaps obtained in the Skyrme-HFB calculations at the spherical shape. The strength of the quadrupole particle-hole interaction is determined to reproduce the magnitude of the axial quadrupole deformation β of the Skyrme-HFB minimum. The strengths of the quadrupole-pairing interaction are determined so as to fulfill the self-consistency condition [30]. We use the quadrupole polarization charge $\delta e_{\text{pol}} = 0.5$ for both neutrons and protons when evaluating $E2$ matrix elements. We solve the CHF + LQRPA equations at 3600 β - γ mesh points in the region $0 < \beta < \beta_{\text{max}}$ and $0^\circ < \gamma < 60^\circ$, with $\beta_{\text{max}} = 0.5$ for ³⁰Mg and 0.6 for ^{32,34,36}Mg.

Our theoretical framework is quite general and it can be used in conjunction with various Skyrme forces/modern density functionals going beyond the P+Q model. Then the effects of weakly bound neutrons and coupling to the continuum on the properties of the low-lying collective excitations, discussed in Refs. [14, 15], can be taken into account, for example, by solving the CHF + LQRPA equations in the 3D coordinate mesh representation. However, it requires a large-scale calculation with modern parallel processors and it remains as a challenging future subject. A step toward this goal has recently been carried out for axially symmetric cases [26].

Figure 1 shows the collective potentials $V(\beta, \gamma)$ for ^{30–36}Mg. It is clearly seen that prolate deformation grows with increase of the neutron number. The collective potential for ³⁰Mg is very soft with respect to β . It has a minimum at $\beta = 0.11$ and a local minimum at $\beta = 0.33$. The barrier height between the two minima is only 0.24 MeV (measured from the lower minimum). In ³²Mg, in addition to the prolate minimum at $\beta = 0.33$, a spherical local minimum (associated with the $N = 20$ spherical shell gap) appears. The barrier height between the two minima is 1.0 MeV (measured from the lower minimum). The spherical local minimum disappears in ³⁴Mg and ³⁶Mg, and the prolate minima become soft in the direction of triaxial deformation γ . In ³⁴Mg, the potential minimum is located at $\gamma = 10^\circ$.

In Fig. 2, calculated excitation energies and $E2$ transition strengths are compared with the experimental data. The lowering of the excitation energies of the 2_1^+ and 4_1^+ states and the remarkable increase of $B(E2; 2_1^+ \rightarrow 0_1^+)$ from ³⁰Mg to ³⁴Mg are well described in this calculation. The calculated ratio of the excitation energies, $E(4_1^+)/E(2_1^+)$, increases as 2.37, 2.82, 3.26, and 3.26, while the ratio of the transition strengths, $B(E2; 4_1^+ \rightarrow 2_1^+)/B(E2; 2_1^+ \rightarrow 0_1^+)$, decreases as 2.03, 1.76, 1.43, and

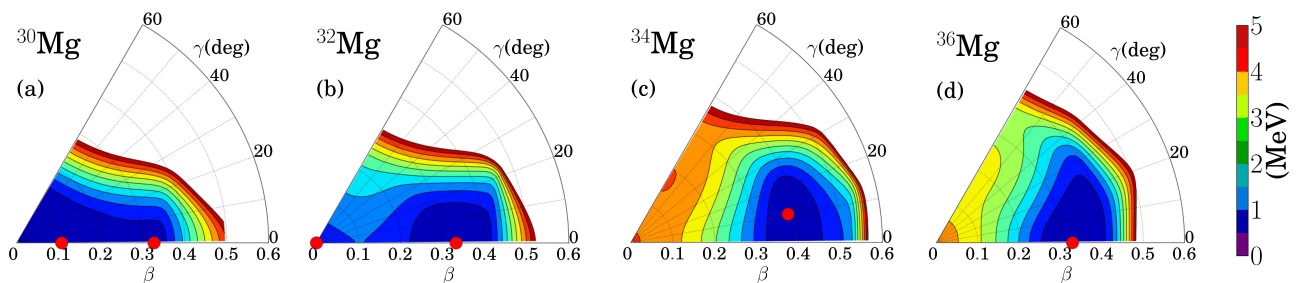


FIG. 1: (Color online) Collective potentials for $^{30-36}\text{Mg}$. The HFB equilibrium points are indicated by red circles.

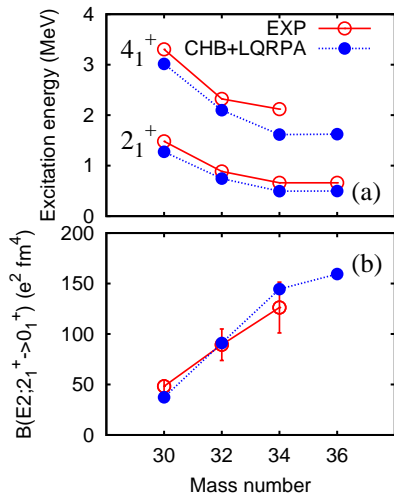


FIG. 2: (Color online) Comparison of calculated excitation energies of the 2_1^+ and 4_1^+ states (upper panel) and $B(E2; 2_1^+ \rightarrow 0_1)$ values (lower panel) in $^{30-36}\text{Mg}$ with experimental data [1–6].

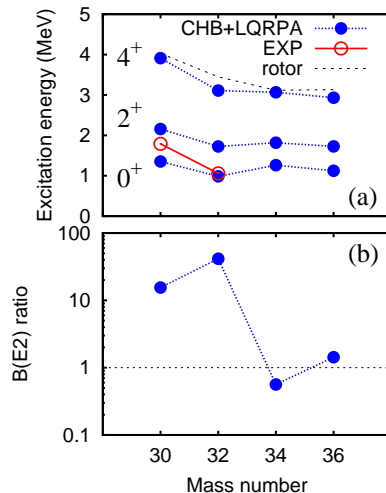


FIG. 3: (Color online) Excitation energies of the excited 0_2^+ , $2_{2,3}^+$ and $4_{2,3}^+$ states (upper panel) and the ratio $B(E2; 0_2^+ \rightarrow 2_1^+)/B(E2; 0_1^+ \rightarrow 2_{2,3}^+)$ of the inter-band $E2$ transition strengths between the $K = 0_2$ and $K = 0_1$ bands (lower panel). Experimental data are taken from Refs. [21, 22]. See texts for details.

1.47, in going from ^{30}Mg to ^{36}Mg . Thus, the properties of the 2_1^+ and 4_1^+ states gradually change from vibrational to rotational with increasing neutron number.

Let us next discuss the properties of the 0_2^+ states and the 2^+ and 4^+ states connected to the 0_2^+ states with strong $E2$ transitions. The result of calculation is presented in Fig. 3 together with the recent experimental data. The calculated excitation energies of the 0_2^+ states are 1.353 and 0.986 MeV for ^{30}Mg and ^{32}Mg , respectively, in fair agreement with the experimental data [21, 22]. In particular, the very low excitation energy of the 0_2^+ state in ^{32}Mg is well reproduced. In our calculation, more than 90% (80%) of the collective wave functions for the yrast (excited) band members are composed of the $K = 0$ component. Therefore we denote the ground band by ‘the $K = 0_1$ band,’ and the excited band by ‘the $K = 0_2$ band.’ The 2^+ and 4^+ states belonging to the $K = 0_2$ band appear as the second 2^+ and 4^+ states in $^{30,32}\text{Mg}$, while they appear as the third 2^+ and 4^+ states in $^{34,36}\text{Mg}$. Accordingly, we use $2_{2,3}^+$ and $4_{2,3}^+$, to collec-

tively indicate the second or the third 2^+ and 4^+ states. The calculated ratios of the excitation energies relative to the excited 0_2^+ state, $[E(4_{2,3}^+) - E(0_2^+)]/[E(2_{2,3}^+) - E(0_2^+)]$, are 3.18, 2.87, 3.25, and 3.00, for ^{30}Mg , ^{32}Mg , ^{34}Mg , and ^{36}Mg , respectively. In the upper panel of Fig. 3 we also plot the rotor-model prediction for the excitation energies of the 4^+ states estimated from the $0^+ - 2^+$ spacings in the $K = 0_2$ bands. The deviation from the rotor-model prediction is largest in ^{32}Mg indicating importance of shape-fluctuation effects. Although the calculated excitation spectrum of the $K = 0_2$ band in ^{30}Mg looks rotational, we find a significant deviation from the rotor-model prediction in the $E2$ transition properties. The calculated ratios of the $E2$ transition strengths, $B(E2; 4_{2,3}^+ \rightarrow 2_{2,3}^+)/B(E2; 2_{2,3}^+ \rightarrow 0_2^+)$, are 1.05, 1.54, 1.47, and 1.51, for $^{30-36}\text{Mg}$, respectively. The deviation from the rotor-model value (1.43) is largest in ^{30}Mg . The significant deviation from the simple rotor-model pat-

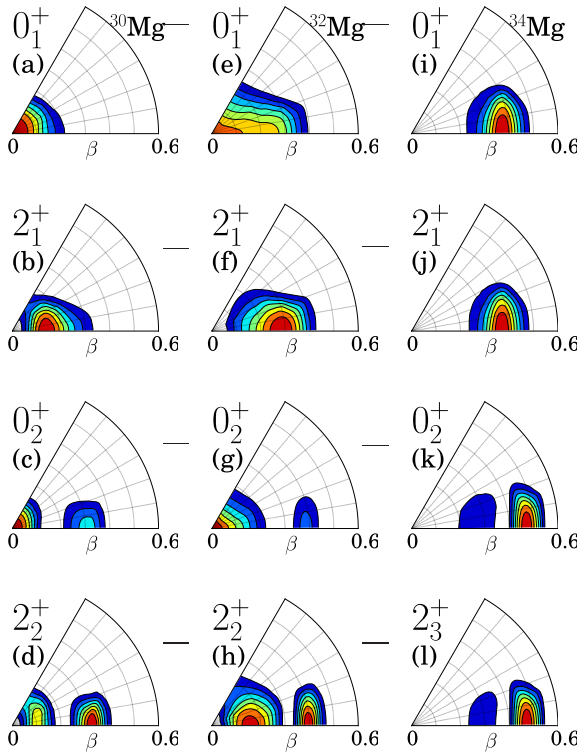


FIG. 4: (Color online) Vibrational wave functions squared $\sum_K |\Phi_{\alpha IK}(\beta, \gamma)|^2$ of the 0_1^+ , 2_1^+ , 0_2^+ and $2_{2,3}^+$ states in $^{30-34}\text{Mg}$. Contour lines are drawn at every eighth part of the maximum value.

tern of the $K = 0_2$ bands in ^{30}Mg and ^{32}Mg , noticed above, can be seen more drastically in the inter-band $E2$ transition properties. In the lower panel of Fig. 3, we plot the ratio $B(E2; 0_2^+ \rightarrow 2_1^+)/B(E2; 0_1^+ \rightarrow 2_{2,3}^+)$ of the inter-band transition strengths between the $K = 0_1$ and $K = 0_2$ bands. If the $K = 0_1$ and $K = 0_2$ bands are composed of only the $K = 0$ component and the intrinsic structures in the (β, γ) plane are the same within the band members, this ratio should be one. These ratios for ^{34}Mg and ^{36}Mg are close to one, indicating that the change of the intrinsic structure between the 0^+ and 2^+ states is small. In contrast, the ratios for ^{30}Mg and ^{32}Mg are larger than 10, indicating a remarkable change in the shape-fluctuation properties between the 0^+ and 2^+ states belonging to the $K = 0_1$ and $K = 0_2$ bands.

Figure 4 shows the vibrational wave functions squared $\sum_K |\Phi_{\alpha IK}(\beta, \gamma)|^2$. Let us first examine the character change of the ground state from ^{30}Mg to ^{34}Mg . In ^{30}Mg , the vibrational wave function of the ground 0_1^+ state is distributed around the spherical shape. In ^{32}Mg , it is remarkably extended to the prolately deformed region. In ^{34}Mg , it is distributed around the prolate shape. From the behavior of the vibrational wave functions, one can conclude that shape fluctuation in the ground 0_1^+ state is largest in ^{32}Mg . To understand the microscopic mechanism of this change from ^{30}Mg to ^{34}Mg , it is necessary to

take into account not only the properties of the collective potential in the β direction but also its curvature in the γ direction and the collective kinetic energy (collective masses). This point will be discussed in our forthcoming full-length paper. As suggested from the behavior of the inter-band $B(E2)$ ratio, the vibrational wave functions of the 2_1^+ state are noticeably different from those of the 0_1^+ state in ^{30}Mg and ^{32}Mg , while they are similar in the case of ^{34}Mg . Next, let us examine the vibrational wave functions of the 0_2^+ and $2_{2,3}^+$ states in $^{30-34}\text{Mg}$. It is immediately seen that they exhibit one node in the β direction. This is their common feature. In ^{30}Mg and ^{32}Mg , one bump is seen in the spherical to weakly-deformed region, while the other bump is located in the prolately deformed region around $\beta = 0.3 - 0.4$. In ^{34}Mg , the node is located near the peak of the vibrational wave function of the 0_1^+ state, suggesting that they have β -vibrational properties.

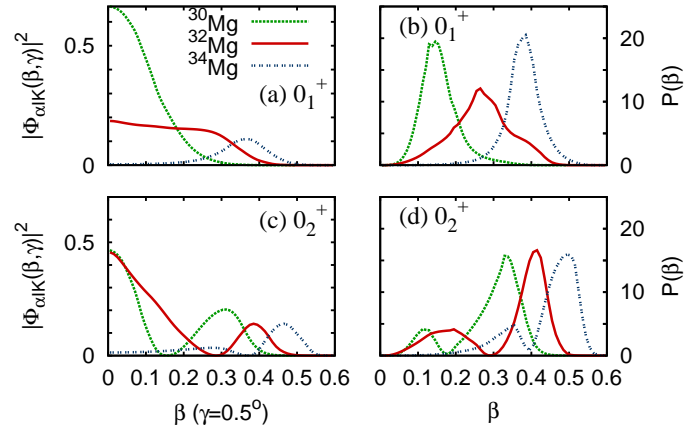


FIG. 5: (Color online) (a) Vibrational wave functions squared, $|\Phi_{\alpha, I=0, K=0}(\beta, \gamma = 0.5^\circ)|^2$, of the 0_1^+ states in $^{30-34}\text{Mg}$. Their values along the $\gamma = 0.5^\circ$ line are plotted as functions of β . (b) Probability densities integrated over γ , $P(\beta) \equiv \int d\gamma |\Phi_{\alpha, I=0, K=0}(\beta, \gamma)|^2 |G(\beta, \gamma)|^{1/2}$, of the 0_1^+ states in $^{30-34}\text{Mg}$, plotted as functions of β . (c) Same as (a) but for the 0_2^+ states. (d) Same as (b) but for the 0_2^+ states.

To further reveal the nature of the ground and excited 0^+ states, it is important to examine not only their vibrational wave functions but also their probability density distributions. Since the 5D collective space is a curved space, the normalization condition for the vibrational wave functions is given by

$$\int \sum_K |\Phi_{\alpha IK}(\beta, \gamma)|^2 |G(\beta, \gamma)|^{1/2} d\beta d\gamma = 1 \quad (5)$$

with the volume element

$$|G(\beta, \gamma)|^{1/2} d\beta d\gamma = 2\beta^4 \sqrt{W(\beta, \gamma) R(\beta, \gamma)} \sin 3\gamma d\beta d\gamma, \quad (6)$$

$$W(\beta, \gamma) = \{D_{\beta\beta}(\beta, \gamma)D_{\gamma\gamma}(\beta, \gamma) - [D_{\beta\gamma}(\beta, \gamma)]^2\}\beta^{-2}, \quad (7)$$

$$R(\beta, \gamma) = D_1(\beta, \gamma)D_2(\beta, \gamma)D_3(\beta, \gamma), \quad (8)$$

where $D_{k=1,2,3}$ are the rotational masses defined through $\mathcal{J}_k = 4\beta^2 D_k \sin^2(\gamma - 2\pi k/3)$. Thus, the probability density of taking a shape with specific values of (β, γ) is given by $\sum_K |\Phi_{\alpha IK}(\beta, \gamma)|^2 |G(\beta, \gamma)|^{1/2}$. Due to the β^4 factor in the volume element, the spherical peak of the vibrational wave function disappears in the probability density distribution. Accordingly, it will give us a picture quite different from that of the wave function. Needless to say, it is important to examine both aspects to understand the nature of individual quantum states.

In Fig. 5, we display the probability density integrated over γ , $P(\beta) \equiv \int d\gamma |\Phi_{\alpha, I=0, K=0}(\beta, \gamma)|^2 |G(\beta, \gamma)|^{1/2}$, of finding a shape with a specific value of β , together with the vibrational wave functions squared $|\Phi_{\alpha, I=0, K=0}(\beta, \gamma)|^2$ for the ground and excited 0^+ states ($\alpha = 1$ and 2). Let us first look at the upper panels for the ground states. We note that, as expected, the spherical peak of the vibrational wave function for ^{30}Mg in Fig. 5(a) corresponds to the peak at $\beta \simeq 0.15$ of the probability density in Fig. 5(b). In Fig. 5(b), the peak position moves toward a larger value of β in going from ^{30}Mg to ^{34}Mg . The distribution for ^{32}Mg is much broader than those for ^{30}Mg and ^{34}Mg .

Next, let us look at the lower panels in Fig. 5 for the excited states. In Fig. 5(c), the vibrational wave functions for ^{30}Mg and ^{32}Mg exhibit the maximum peak at the spherical shape. However, these peaks become small and are shifted to the region with $\beta \simeq 0.1$ and $\beta \simeq 0.2$ in ^{30}Mg and ^{32}Mg , respectively, in Fig. 5(d). On the other hand, the second peaks at $\beta \simeq 0.3$ and $\beta \approx 0.4$ in ^{30}Mg and ^{32}Mg , respectively, seen in Fig. 5(c) become the prominent peaks in Fig. 5(d). In ^{30}Mg , the bump at $\beta \simeq 0.1$ is much smaller than the major bump around $\beta \simeq 0.3$. In this sense, we can regard the 0_2^+ state of ^{30}Mg as a prolately deformed state. In the case of ^{32}Mg , the probability density exhibits a very broad distribution

extending from the spherical to deformed regions up to $\beta = 0.5$ with a prominent peak at $\beta \simeq 0.4$ and a node at $\beta \simeq 0.3$. The position of the node coincides with the peak of the probability density distribution of the 0_1^+ state, as expected from the orthogonality condition. The range of the shape fluctuation of the 0_2^+ state in β direction is almost the same as that of the 0_1^+ state. Thus, the result of our calculation yields a physical picture for the 0_2^+ state in ^{32}Mg that is quite different from the ‘spherical excited 0^+ state’ interpretation based on the inversion picture of the spherical and deformed configurations. In ^{34}Mg , the peak is shifted to the region with a larger value of β and the tail toward the spherical shape almost disappears.

In summary, we have investigated the large-amplitude collective dynamics in the low-lying states of $^{30-36}\text{Mg}$ by solving the 5D quadrupole collective Schrödinger equation. The collective masses and potentials of the 5D collective Hamiltonian are microscopically derived with use of the CHF + LQRPA method. Good agreement with the recent experimental data is obtained for the excited 0^+ states as well as the ground bands. For ^{30}Mg , the shape coexistence picture that the deformed excited 0^+ state coexists with the spherical ground state approximately holds. On the other hand, large-amplitude quadrupole-shape fluctuations dominate in both the ground and the excited 0^+ states in ^{32}Mg , so that the interpretation of ‘deformed ground and spherical excited 0^+ states’ based on the simple inversion picture of the spherical and deformed configurations does not hold. To test these theoretical predictions, experimental search for the distorted rotational bands built on the excited 0_2^+ states in ^{30}Mg and ^{32}Mg is strongly desired.

One of the authors (N. H.) is supported by the Special Postdoctoral Research Program of RIKEN. The numerical calculations were performed on the RIKEN Integrated Cluster of Clusters (RICC). This work is supported by KAKENHI (Nos. 21340073, 20105003, 23540234, and 23740223).

-
- [1] A. N. Deacon *et al.*, Phys. Rev. C **82**, 034305 (2010).
[2] S. Takeuchi *et al.*, Phys. Rev. C **79**, 054319 (2009).
[3] K. Yoneda *et al.*, Phys. Lett. B **499**, 233 (2001).
[4] O. Niedermaier *et al.*, Phys. Rev. Lett. **94**, 172501 (2005).
[5] T. Motobayashi *et al.*, Phys. Lett. B **346**, 9 (1995).
[6] H. Iwasaki *et al.*, Phys. Lett. B **522**, 227 (2001).
[7] E. K. Warburton *et al.*, Phys. Rev. C **41**, 1147 (1990).
[8] Y. Utsuno *et al.*, Phys. Rev. C **60**, 054315 (1999).
[9] E. Caurier *et al.*, Nucl. Phys. A **693**, 374 (2001).
[10] T. Otsuka, Eur. Phys. J. A **20**, 69 (2003).
[11] J. Terasaki *et al.*, Nucl. Phys. A **621**, 706 (1997).
[12] P.-G. Reinhard *et al.*, Phys. Rev. C **60**, 014316 (1999).
[13] H. Ohta *et al.*, Eur. Phys. J. A **25**, s1.549 (2005).
[14] M. Yamagami *et al.*, Phys. Rev. C **69**, 034301 (2004).
[15] K. Yoshida *et al.*, Phys. Rev. C **77**, 044312 (2008).
[16] R. Rodríguez-Guzmán *et al.*, Nucl. Phys. A **709**, 201 (2002).
[17] J. M. Yao *et al.*, Phys. Rev. C **83**, 014308 (2011).
[18] J. M. Yao *et al.*, Int. J. Mod. Phys. E **20**, 482 (2011).
[19] M. Kimura *et al.*, Prog. Theor. Phys. **107**, 33 (2002).
[20] H. Mach *et al.*, Eur. Phys. J. A **25**, 105 (2005).
[21] W. Schwerdtfeger *et al.*, Phys. Rev. Lett. **103**, 012501 (2009).
[22] K. Wimmer *et al.*, Phys. Rev. Lett. **105**, 252501 (2010).
[23] N. Hinohara *et al.*, Phys. Rev. C **82**, 064313 (2010).
[24] K. Sato *et al.*, Nucl. Phys. A **849**, 53 (2011).
[25] N. Hinohara *et al.*, Phys. Rev. C **83**, 014321 (2011).
[26] K. Yoshida *et al.*, Phys. Rev. C **83**, 061302 (2011).
[27] N. Hinohara *et al.*, AIP Conf. Proc. **1355**, 200 (2011), arXiv:1101.2256.

- [28] M. Stoitsov *et al.*, *Comp. Phys. Comm.* **167**, 43 (2005). [30] H. Sakamoto *et al.*, *Phys. Lett. B* **245**, 321 (1990).
[29] T. Bengtsson *et al.*, *Nucl. Phys. A* **436**, 14 (1985).